Contents lists available at ScienceDirect

BBA - General Subjects

journal homepage: www.elsevier.com/locate/bbagen

Characterisation of biocondensate microfluidic flow using array-detector FCS

Stijn Dilissen [a,b,1], Pedro L. Silva [a,1], Anastasia Smolentseva [a], Tom Kache [a], Ronald Thoelen [b,c], Jelle Hendrix [a,*]

[a] UHasselt, Dynamic Bioimaging Lab, Advanced Optical Microscopy Centre, Biomedical Research Institute, Agoralaan C (BIOMED), B3590 Diepenbeek, Belgium
[b] UHasselt, Biomedical Device Engineering group, Institute for Materials Research (IMO-IMOMEC), Wetenschapspark 1, B3590 Diepenbeek, Belgium
[c] IMOMEC Division, IMEC vzw, Wetenschapspark 1, B3590 Diepenbeek, Belgium

A B S T R A C T

Background: Biomolecular condensation via liquid-liquid phase separation (LLPS) is crucial for orchestrating cellular activities temporospatially. Although the rheological heterogeneity of biocondensates and the structural dynamics of their constituents carry critical functional information, methods to quantitatively study biocondensates are lacking. Single-molecule fluorescence research can offer insights into biocondensation mechanisms. Unfortunately, as dense condensates tend to sink inside their dilute aqueous surroundings, studying their properties via methods relying on Brownian diffusion may fail.
Methods: We take a first step towards single-molecule research on condensates of Tau protein under flow in a microfluidic channel of an in-house developed microfluidic chip. Fluorescence correlation spectroscopy (FCS), a well-known technique to collect molecular characteristics within a sample, was employed with a newly commercialised technology, where FCS is performed on an array detector (AD-FCS), providing detailed diffusion and flow information.
Results: The AD-FCS technology allowed characterising our microfluidic chip, revealing 3D flow profiles. Subsequently, AD-FCS allowed mapping the flow of Tau condensates while measuring their burst durations through the stationary laser. Lastly, AD-FCS allowed obtaining flow velocity and burst duration data, the latter of which was used to estimate the condensate size distribution within LLPS samples.
Conclusion: Studying biocondensates under flow through AD-FCS is promising for single-molecule experiments. In addition, AD-FCS shows its ability to estimate the size distribution in condensate samples in a convenient manner, prompting a new way of investigating biocondensate phase diagrams.
General significance: We show that AD-FCS is a valuable tool for advancing research on understanding and characterising LLPS properties of biocondensates.

1. Introduction

Biological liquid-liquid phase separation (LLPS) is a colloidal process by which dynamic liquid-like droplets of concentrated biomolecules are spontaneously and reversibly formed in solution and cells [1]. Over the last decade, it has become clear that such processes are essential in maintaining physiological conditions, being functionally involved in a plethora of biological processes such as, but not limited to, RNA metabolism, gene transcription, cell signalling, stress response, sensing, and cell division [2]. Besides these functions, LLPS has been associated with

diseases such as dementia and cancer [3]. Membrane-less organelles (MLOs) comprise intrinsically disordered proteins (IDPs) and often RNA. While in vivo MLOs typically contain tens to hundreds of different types of IDPs and RNA, in vitro condensates can also be formed from a single type of IDP under the right experimental conditions.

The microtubule-associated protein Tau (often abbreviated to as MAPT) is an IDP that is composed of a negatively charged N- and C-terminus, while its central (proline-rich and microtubule-binding) regions are highly positively charged. Tau is abundantly expressed in the central nervous system and is vital for stabilising the microtubule

cytoskeleton [4,5]. Besides its function in cellular healthy conditions, Tau is infamous for its propensity to form intracellular aggregates. These aggregates are involved in the progression of specific types of dementia named Tauopathies, such as Alzheimer's disease, Pick's disease, and corticobasal degeneration. Interestingly, a conformational change has been found in Tau when incorporated into such aggregates, with the microtubule-binding region adopting a more rigid and collapsed conformation, while the N- and C-termini remain largely disordered. Furthermore, the conformation of aggregates is disease-specific [6–9]. Therefore, conformational changes might be at the core of disease onset and progression.

Tau can condense in cellular and in vitro models in the presence of negatively charged molecules, such as RNA, or crowding agents, such as polyethylene-glycol (PEG) [10]. While this process may be helpful for high protein concentration storage and for facilitating interaction with microtubules, the difference in local concentration and physical micro-environment might cause individual proteins to adopt aggregation-prone conformations [11,12]. Moreover, Wen et al. (2021), with the use of single-molecule Förster resonance energy transfer (smFRET), reported an overall extended conformation of Tau when integrated into biocondensates [13]. Partitioning in a condensed phase can, therefore, be a pathological pathway for Tauopathies, and thus, revealing intermediate conformations is crucial to understand aggregation mechanisms.

In an environment where thousands of proteins are present, ensemble molecular structural methodologies reveal an average conformation of the system, therefore overlooking proteins adopting specific transient and steady conformational states. Applying single-molecule techniques is more suitable for protein studies inside biocondensates. Burstwise smFRET is a confocal single-molecule fluorescence technique where a distance-dependent energy transfer occurs from a donor dye to an acceptor dye while molecules freely diffuse by Brownian motion [14], though particular challenges remain. Condensates have a higher density than the surrounding environment [15], causing them to sink in solution and, therefore, to be unable to diffuse through the stationary laser confocal volume. Successful approaches where moving the laser to individual stationary droplets have been carried out before by *N. Galvanetto* et al. *(2023)*. However, this can be time-consuming unless the process is automated, and the long laser exposure times can potentially lead to photobleaching of the fluorescent dyes [16]. Microfluidic chips are platforms featuring micrometre-sized channels that have gained popularity in biomedical research. Owing to the high analytical throughput, versatility of microfluidic chips, compact dimensions that enable investigating different processes at once, and reduced experiment times, they have become an important tool in biomedical sciences with applications ranging from diagnosis, cell studies, and droplet formation, among others [17–19]. In the context of LLPS, microfluidic chips have been used for determining condensate phase diagrams, studying the formation kinetics and properties of condensates, and investigating the single-molecule level interaction of poly-L-lysine and peptides with nucleic acids in the early stage of the LLPS process [20–22].

Fluorescence correlation spectroscopy (FCS) uses the temporal correlation of fluorescence intensity fluctuations at the microseconds to seconds timescale as measured on a confocal microscope to determine the diffusion constant and molar concentration of fluorescently labelled molecules diffusing through the confocal observation volume [23,24]. The use of FCS for studies of solutions under flow was first introduced by *D. Magde* et al. *(1978)* [25]. While single-focus FCS using a single point detector is useful for determining the velocity of a fluorescent solution, it provides no information on directionality of the flow, which can be essential for detailed microfluidic characterisation. Scanning correlation modes that can provide information on both diffusion rates and direction have since been developed. Raster image correlation spectroscopy (RICS) and line-scanning pair-correlation function (pCF) are diffusion-based scanning techniques where the sample is scanned either frame-

wise or line-wise, and diffusion can be determined by spatially correlating pixel fluorescence intensities [26,27]. Other approaches to pCF include the use of two stationary confocal volumes at a known distance or using a single confocal volume excitation with detection over an array of detectors [28]. *Arbour T.J. & Enderlein J. (2010)* demonstrated the use of dual-excitation to determine the flow velocities of Oregon Green 488 in a microfluidic chip [29]. *L. Scipioni* et al. *(2018)* described the use of detection on a detector array using a commercial confocal microscope to determine eGFP diffusion in different cellular compartments [30]. Recently, *Slenders E.* et al. *(2023)* used a home-built single-photon counting detector array approach to determine the diffusion of GFP and Alexa-Fluor 488 [31]. A similar approach to L. *Scipione* et al. *(2018)*, namely the *ZEISS Dynamics Profiler*, has recently been made commercially available [32]. Here, molecular diffusion studies are done by auto-correlating the sum of the fluorescence intensities over the 19 inner elements of the detector array, while flow movements are determined by cross-correlation between detector elements and in specific directions, thereby providing information on diffusion, concentration, flow velocity, flow direction and/or diffusion barriers in a straightforward manner.

Here, we show the utilisation of a straight microfluidic channel combined with the array-detector FCS approach for the characterising ensemble and single-molecule microfluidic flow. We determine flow velocity rates and 3D profiles at different pump pressures, and we apply specific flow parameters to achieve a controlled flow of individual Tau LLPS droplets under laminar conditions. This marks an initial step towards single-molecule research of biological condensates under flow.

2. Methods

A *Key Resource Table* can be found in the Supplementary Information section.

2.1. Microfluidics

Microfluidic chips were produced using standard soft-lithography techniques. First, 50 g of SU-8/3050 photoresist (Microresist Technology GmbH, Berlin, Germany) was thinned by mixing it with 10.841 mL of SU-8/2000 thinner (Microresist Technology GmbH, Berlin, Germany), resulting in the solid content equivalent to SU-8/3010. A SU-8 microfluidic mould was then made by spin coating SU-8/3010 (1000 rpm, ramp rate of 300 rpm/s, 30 s) on a Si wafer (100 mm in diameter, 525 μm in thickness, resistivity of 10–20 Ω·cm) (Neyco, Vanves, France) to achieve a photoresist thickness of 15 μm. Following a soft bake at 95 °C for 10 min on a hotplate, the wafer was UV illuminated for 1 min with a mask aligner (350 nm, 25 mW/cm^2) (KarlSuss MA56 M, SÜSS MICROTEC SE, Garching, Germany) containing a chrome mask (Delta Mask B.V., Enschede, Netherlands). This mask contained a self-designed microfluidic chip pattern created using AUTOCAD 2024 (Autodesk Inc., San Francisco, USA). After a post-exposure bake on a hotplate for 5 min at 95 °C, the wafer was developed using SU-8 developer (Microresist Technology GmbH, Berlin, Germany), rinsed with isopropanol, and dried using N_2. To create the microfluidic chip, a PDMS elastomer base and curing agent (SYLGARD™ 184, Dow Europe Gmbh, Horgen, Switzerland) were mixed 10:1 by weight and poured on top of the master mould. The master was cured overnight in an oven at 70 °C. PDMS microfluidic devices were extracted from the mould and rinsed with isopropanol. PDMS-glass bonding was achieved by exposing the PDMS chip and a clean glass coverslip (24 × 65 mm, #1,5, Menzel-Gläser) to UV ozone for 45 min (Novascan Technologies Inc., Boone, USA). The PDMS chip and the glass were joined and left in an oven at 70 °C overnight to form a covalent bond.

2.2. Microfluidic simulations

To quantitatively evaluate the expected flow and velocity field induced by a pressure gradient, the fluid flow within the microfluidic

channel was simulated using the laminar flow module in COMSOL Multiphysics 5.3 (COMSOL Inc., Burlington, USA). To generate a 3D flow simulation, the 2D model developed for the chrome mask was imported into COMSOL and extruded into a 3D model. Specific material boundaries (glass, PDMS) were defined to mimic the actual flow condition. Simulations were conducted using the steady-state Navier-Stokes model, assuming Newtonian fluid behaviour, no-slip boundary conditions, and incompressible flow within the channel. Because the pressure pump was positioned 24.5 cm lower than the microfluidic chip, the inlet pressure was adjusted to the theoretical pressure at the chip inlet using the Bernoulli equation:

$$P_{Chip} = P_{Pump} - (\rho \cdot g \cdot h), \tag{1}$$

where P_{Chip} is the static pressure at the chip, P_{Pump} is the static pump pressure, ρ is the density of the fluid (water at 23 °C, 997.62 kg/m^3), g is the acceleration due to gravity, and h (m) is the height difference (0.245 m) between pump and chip, with the latter positioned higher. The inlet pressures (P_{Chip}) used were 38.5, 101, and 226 mbar relative to the outlet. The outlet pressure was assumed to be zero. Further details are available in the supplementary materials (S. Table 1). 3D model surface plots, which show the fluid velocity profile, were generated by solving the Navier-Stokes equation. These pressure-driven Δp (Pa) flow velocity profiles $v(x,z)$ in a cross-sectional (x,z) plane of a rectangular channel with length L (m) and where the channel is wider than its height ($h < w$), are analytically expressed in terms of a Fourier series [33]:

$$v(xz) = \frac{\Delta p}{2 \cdot \mu \cdot L} \left\{ \left[\left(\frac{h}{2} \right)^2 - z^2 \right] - \sum_{n=0}^{\infty} a_n \cdot cos\left(\frac{\lambda_n \cdot z}{\frac{h}{2}} \right) \cdot cosh\left(\frac{\lambda_n \cdot x}{\frac{h}{2}} \right) \right\}, \tag{2}$$

where $\lambda_n = \frac{(2n+1)\pi}{2}$

and $a_n = \frac{h^2(-1)^n}{\left[(\lambda_n)^3 \cdot cosh\left(\frac{\lambda_n \cdot w}{h} \right) \right]}$,

and where $v(x,z)$ is the flow velocity along the flow direction at position $(-w/2 < x < w/2, -h/2 < z < h/2)$ orthogonal to the flow direction, with h (m) the channel height, μ (kg·m^{-1}·s^{-1}) the dynamic viscosity of the fluid (water at 23 °C, 0.000933 kg·m^{-1}·s^{-1}) [47], and n the number eigenvalues. The coefficients a_n follow from the no-slip boundary conditions at $x = \pm w/2$, with w (m) the channel width. The corresponding volumetric flow rate of the simulations could then be calculated by integrating Eq. (2) over the channel's area:

$$Q_{sim} = \int_{-w/2}^{w/2} \int_{-h/2}^{h/2} v(xz) dz \, dx. \tag{3}$$

The Reynolds numbers (Re), which define the ratio between the inertial and viscous forces, were calculated using:

$$Re = \frac{\rho \cdot v \cdot L}{\mu}, \tag{4}$$

where ρ (kg/m^3) is the density of the fluid (water at 23 °C, 997.62 kg/m^3), v (m/s) the characteristic velocity of the flow, and μ (kg·m^{-1}·s^{-1}) the dynamic viscosity of the fluid (water at 23 °C, 0.000933 kg·m^{-1}·s^{-1}) [47], and L (m) the "characteristic length", which is equal to the hydraulic diameter (d_H) for rectangular channels:

$$d_H = \frac{2wh}{(w+h)} \tag{5}$$

The hydraulic resistance for the fluid flowing through the microfluidic chip design can be derived using the following formula [34]:

$$R_h = \frac{\Delta p}{Q} \approx \frac{12 \cdot \mu \cdot L}{wh^3 \left(1 - \frac{0.630h}{w} \right)}, \tag{6}$$

where Δp (Pa) is the pressure over the channel (inlet pressure to outlet pressure), Q (m^3/s) is the flow rate, h (m) is the channel height, w (m) is the channel width, μ (kg/m·s) the dynamic viscosity of the fluid (water at 23 °C, 0.000933 kg·m^{-1}·s^{-1}) [47] and L (m) the channel length.

2.3. Protein purification

First, *E. coli* BL21(DE3) CodonPlus RIL (Agilent, Santa Clara, USA) were transformed with the plasmid tau/pET29b, (Addgene plasmid #16316 contributed by Peter Klein (University of Pennsylvania School of Medicine, Philadelphia); http://n2t.net/addgene:16316; RRID: Addgene_16,316) [35], which encodes for full-length 2N4R human Tau protein. Briefly, 20 ng of plasmid was added to 20 μL of chemically-competent *E. coli* cell suspension, and a heat shock was performed at 42 °C for approximately 45 s. Afterwards, 10 volumes of LB medium were added, and the bacteria were allowed to recover at 37 °C for at least 30 min. The bacterial suspension was spread over LB agar plates containing 50 μg/mL kanamycin and incubated overnight at 37 °C. Colonies were picked and incubated overnight, at 37 °C and 180 rpm, in 5 mL LB broth containing 50 μg/mL of kanamycin. Finally, the overnight culture was added to terrific broth (Carl Roth, Karlsruhe, Germany) containing 50 μg/mL of kanamycin in 1:100 and incubated until OD$_{600}$ = 0.6. Protein expression was induced by the addition of 0.2 mM of Isopropyl β- d-1-thiogalactopyranoside (IPTG; Carl Roth, Karlsruhe, Germany), and the cultures were incubated for two more hours. Bacteria were collected by centrifugation and stored at −20 °C until purification. To purify Tau protein, the bacterial pellet was resuspended in 20 mM PIPES (pH 6.3), 15 mM NaCl, 1 mM EDTA, 1 mM MgSO$_4$, 1 mM DTT and disrupted by ultrasonication (SFX250 Digital Sonifier Cell Disruptor 101–063-965R / 101–063-966R, Branson, Danbury, USA) on an ice-water bath for 10 min (0.5 s intervals) at 70 W. The lysate was centrifuged at 10,000 *g* and 4 °C, and the resulting supernatant boiled for 10 min to precipitate folded proteins in the bacterial lysate. Precipitated protein was removed by another round of centrifugation. The protein was purified further from the supernatant by cation exchange chromatography (HiTrap Capto SP Impres 5 mL; Cytiva, Marlborough, USA) on an FPLC (AKTA Pure 25, Cytiva) and eluted with a linear NaCl gradient to 0.5 M over 10 column volumes. Tau protein eluted from the column with approximately 200 mM NaCl. The presence and purity of Tau protein was checked by SDS-PAGE and Coomassie staining. Fractions containing the protein were pooled and concentrated using a 10 kDa microcentrifuge concentrator (Merck KGaA, Darmstadt, Germany). Protein aliquots containing 10% (*V*/V) glycerol were stored at −80 °C. To fluorescently label purified Tau, the protein was buffer exchanged into 10 mM HEPES (pH 7.4), 150 mM NaCl, 1 mM EDTA using a 5 mL HiTrap desalting column (Cytiva, USA) to remove DTT since it will react with the maleimide functionality of the fluorescent dyes. Protein at 100 μM was incubated with Alexa-Fluor 488 C5 maleimide (JenaBiosciences, Jena, Germany) in a 1:3 molar ratio for 2 h at room temperature in a total volume of 100 μL. To remove unreacted dye, a desalting column (PD10, Cytiva, USA) was used to buffer exchange to the HEPES buffer mentioned before, following the manufacturer's protocol. The labelled protein was collected and concentrated with an Amicon-10 k column (Merck KGaA, Darmstadt, Germany). Labelled protein was stored at −80 °C until use.

2.4. Condensate formation

The number and size of condensates is NaCl concentration-dependent. For this reason, purified Tau was first buffer exchanged with a desalting column (HiTrap, Cytiva) and eluted with a pH 7.4 buffer

containing 10 mM HEPES, 10 mM NaCl and 1 mM EDTA. Tau condensation was induced by diluting Tau to 50 μM in a buffer with a final composition of 10 mM HEPES, 10 mM NaCl, and 1 mM EDTA. Also, 15% (*w/V*) polyethylene-glycol 8000 was added as a crowding agent, after this step, the solution was thoroughly mixed to promote the demixing into dilute and dense phases. To enable labelled Tau to be incorporated via diffusion into the intra-droplet environment, it was added as the very last step, after droplet formation, at a concentration of 20 nM.

2.5. AD-FCS-based volumetric flow rate measurements

First, the channels were flushed with 1.5 mL of 70% (*V/V*) pure ethanol followed by 1.5 mL of MQ water at increasing pump pressures to remove any smaller impurities. Subsequently, an 80-nM solution of ATTO 488 carboxy (ATTO-TEC GmbH, Siegen, Germany) was introduced into the channel and ran at constant pump pressures (62.5, 125 and 250 mbar above atmospheric pressure), controlled by a pressure pump (Flow EZ™, Fluigent). In all cases, the outlets were at atmospheric pressure. All images and FCS measurements were conducted with a confocal microscope (LSM 900, Carl Zeiss, Jena, Germany) using a 63× water immersion objective (C-ApoChromat 63×/1.20 W Korr M27, FCS-grade, Zeiss) and an *Airyscan 2* detector. A reference image was made before each FCS measurement. Afterwards, at each height position, ten FCS spots were evenly distributed over the width of the channel. FCS measurements were performed for 15 s per spot with a laser power of approximately 65 μW. Even though the *Airyscan* detector consists of an array of 32 hexagonal detection units, only the inner 19 units are used for FCS, as they have the highest signal-to-noise ratio. Diffusion is determined by correlating fluorescence intensity traces over time with Eq. (8) [32]:

$$G(\tau) = \frac{\langle I(t) \cdot I(t+\tau) \rangle}{\langle I \rangle^2}, \tag{7}$$

where $G(\tau)$ is the amplitude of the correlation curve, $I(t)$ is the (sum of the inner 19 elements') fluorescence intensity, and τ is the time lag for correlation. Data is further fitted with a one-component 3D diffusion model [32]:

$$G(\tau) = A \cdot \left(1 + \frac{T_t \cdot exp^{\frac{-\tau}{\tau_t}}}{1 - T_t}\right) \cdot \left(1 - \frac{\tau}{\tau_d}\right) \cdot \left(1 - \frac{\tau}{\tau_d} \frac{1}{S^2}\right)^{-0.5} + 1, \tag{8}$$

where A is the correlation amplitude, T_t is the triplet fraction, τ_d is the translational diffusion time, and S is the structural parameter defined by $\omega_z/\omega_{r\,FCS}$ with ($S = 5.46$; $\omega_{r\,FCS} = 0.206$), and $\tau_t = 3$ μs is the fixed triplet relaxation time.

To determine flow speed and direction, fluorescence intensity cross-correlation was done bidirectionally along three distinct axes (a total of 6 correlation directions), with each function the average of 9 equidistant pair-correlations of non-adjacent detector elements within the 3 inner detector element rings. The reader is referred to the white paper on the ZEISS Dynamics Profiler for more information. Qualitatively, flow was identified when there was a disparity between the cross-correlation graphs of opposite directions. Quantitatively, all correlation curves were globally fitted using the following model [32]:

$$G(\tau) = A \cdot exp\left(-\frac{r_0^2 + \tau^2 v^2 - 2r_0 \tau v \cdot cos(\phi)}{4D\tau + \omega_{r\,flow}^2}\right) \cdot G_{diff}(\tau) + 1, \tag{9}$$

where v is the flow velocity (fit parameter), ϕ the angle between the flow direction and the vector connecting the detector elements in this group of cross-correlations (fit parameter), r_0 the apparent distance between the detector elements that get cross-correlated with one element in between.

($r_0 = 0.119$ μm), $\omega_{r\,flow}$ is the observation volume radius for an individual detector element, averaged across elements 1 to 19 ($\omega_{r\,flow} =$

0.164 μm), and $G_{diff}(\tau)$ is the diffusion component (Eq. (8) without the A).

Flow velocities of data recorded during the flow of ATTO 488 at different pump pressures could be visualised and retrieved immediately post-measurement in the Zen Blue 3.8 (*Zeiss*) software. Subsequently, these flow velocities were exported and represented in both 2D flow velocity profile plots and 3D model surface plots, revealing the fluid velocity profile. The experimental volumetric flow rate $Q_{exp.}$ was approximated from the measured 2D flow velocity profiles at the half-height of the channel. The average velocity (v_{avg}) along the half-height of the channel $v\left(y, \frac{h}{2}\right)$ was obtained by integrating the measured velocity profiles over the channel width (w):

$$v_{avg} = \frac{1}{w} \int_{-w/2}^{w/2} v\left(x, \frac{h}{2}\right) dx \tag{10}$$

The volumetric flow rate $Q_{exp.}$ was then determined using Eq. (10), where the flow rate is defined by the average flow velocity, the cross-sectional area (A) of the microfluidic channel, and the systematic bias c when $Q_{exp.}$ was calculated from v_{avg} at only one height:

$$Q_{exp} = v_{avg} \cdot A \cdot (1 - c), \quad \text{with} \quad A = w \cdot h. \tag{11}$$

2.6. Tau flow measurements

Full-length Tau protein possesses a theoretical isoelectric point of 7.935, which renders it net positively charged at pH 7.4. Since, at their surfaces, both glass and PDMS have a net negative charge, Tau will likely be prone to adsorption to the surfaces of the microfluidic chip. To minimise this effect, a solution of 1 mg/mL PLL-p-PEG (SuSoS AG, Dübendorf, Switzerland) was pumped through the tubes and channels to create a coating layer. The PLL-g-PEG solution was flushed with a buffer solution of 10 mM HEPES, 150 mM NaCl and 1 mM EDTA at pH 7.4. An 80-nM solution of monomeric Tau labelled with Alexa-Fluor 488-maleimide was then introduced, and flow measurements were performed as described above. Ten FCS spots were evenly distributed across the width of the channel. FCS measurements were conducted at the *z*-height corresponding to the middle of the channel. Each spot was measured for 1 min, with a laser power of 65 μW, as measured in the sample. Finally, Tau condensates were added to the channel, and their flow was captured at pressures ranging from 25 to 1000 mbar. Flow velocities of data recorded for the flow of monomeric Tau protein could be retrieved immediately after measurement. Analysis of the condensed phase and dilute phase of the Tau condensate solution was conducted similarly. To retrieve uncontaminated flow velocity data of the monomeric protein dilute phase, a digital dust filter feature was applied to remove small bright particles, such as biocondensates. This digital filter removed the bright biocondensates from the experimental data when the average intensity multiplied with a custom value (0.8) exceeded the mean signal intensity [32].

To define the ratio of the inertial forces acting on particles, such as biocondensates to the viscous forces of the surrounding flow, the particle Reynolds numbers Re_p, were calculated using [36]:

$$Re_p = \frac{\rho V_s a}{\mu}, \quad \text{with} \quad V_s = v_{max}\left(\frac{a}{d_H}\right), \tag{12}$$

and where ρ (m/s) is the fluid velocity, V_s (m/s) is the shear velocity, a (m) is the particle diameter,

μ (kg·m^{-1}·s^{-1}) the dynamic viscosity of the fluid (Tau LLPS dilute phase at 23 °C, 0.0021970 kg·m^{-1}·s^{-1}), v_{max} (m/s) is the centreline velocity, and d_H (m) is the hydraulic diameter of the microchannel.

Tau droplet diameters were approximated by converting the flow velocity of the dilute phase (v_{flow}) and the burst duration (t_{burst}) of the Tau droplets, with $\omega_{r\,FCS} = 0.206$ μm, into a distance using:

$$\text{Particle diameter} = (v_{flow} \cdot t_{burst}) - (2 \cdot \omega_{r \; FCS}) \qquad (13)$$

2.7. AD-FCS diffusion measurements

The dynamic viscosities of a 15% (*w/V*) polyethylene-glycol 8000 solution, the dilute phase of the Tau LLPS sample, and the dense phase of the Tau LLPS sample were approximated by measuring the diffusivity of ATTO 488 via FCS under atmospheric pressure. Subsequently, the dynamic viscosities could then be calculated by rearranging the Stokes-Einstein equation:

$$\mu = \frac{k \cdot T}{6 \cdot \pi \cdot r \cdot D}, \qquad (14)$$

where μ (kg·m^{-1}·s^{-1}) is the dynamic viscosity of the fluid, k is the Boltzmann constant $(1.38 \cdot 10^{-23} J \cdot K^{-1})$, T is the absolute temperature (K), r is the hydrodynamic radius (for ATTO 488, $6.13 \cdot 10^{-10}$ m) [37] and D the diffusion coefficient for ATTO 488 in the different solutions derived from Eq. (8).

2.8. Data analysis of the Tau biocondensates

The number of biocondensates flowing through the probe volume and their burst duration were accessed and analysed with a home-built script. In short, for every measurement spot, the FCS intensity traces for all 32 detector elements, stored as 8-bit 1024 × 256 images with each pixel representing a 1.2 μs time unit step, were read using the *czi file* Python module (Christoph Gohlke, https://github.com/cgohlke/czifile/). The intensity trace was recovered by summing the signal from the 19 innermost detector elements of the AiryScan detector unit. The initial 5 s of every FCS intensity trace were truncated, and the trace was binned into 12 μs time steps. A custom burst search function was used to extract the burst duration of Tau droplets through the observation volume. In short, a user-specified intensity threshold was set, typically to twice the background noise level, at which a burst start time was marked. Once the intensity had dropped below the threshold for at least three time bins, a burst end was recorded, and the burst duration was calculated.
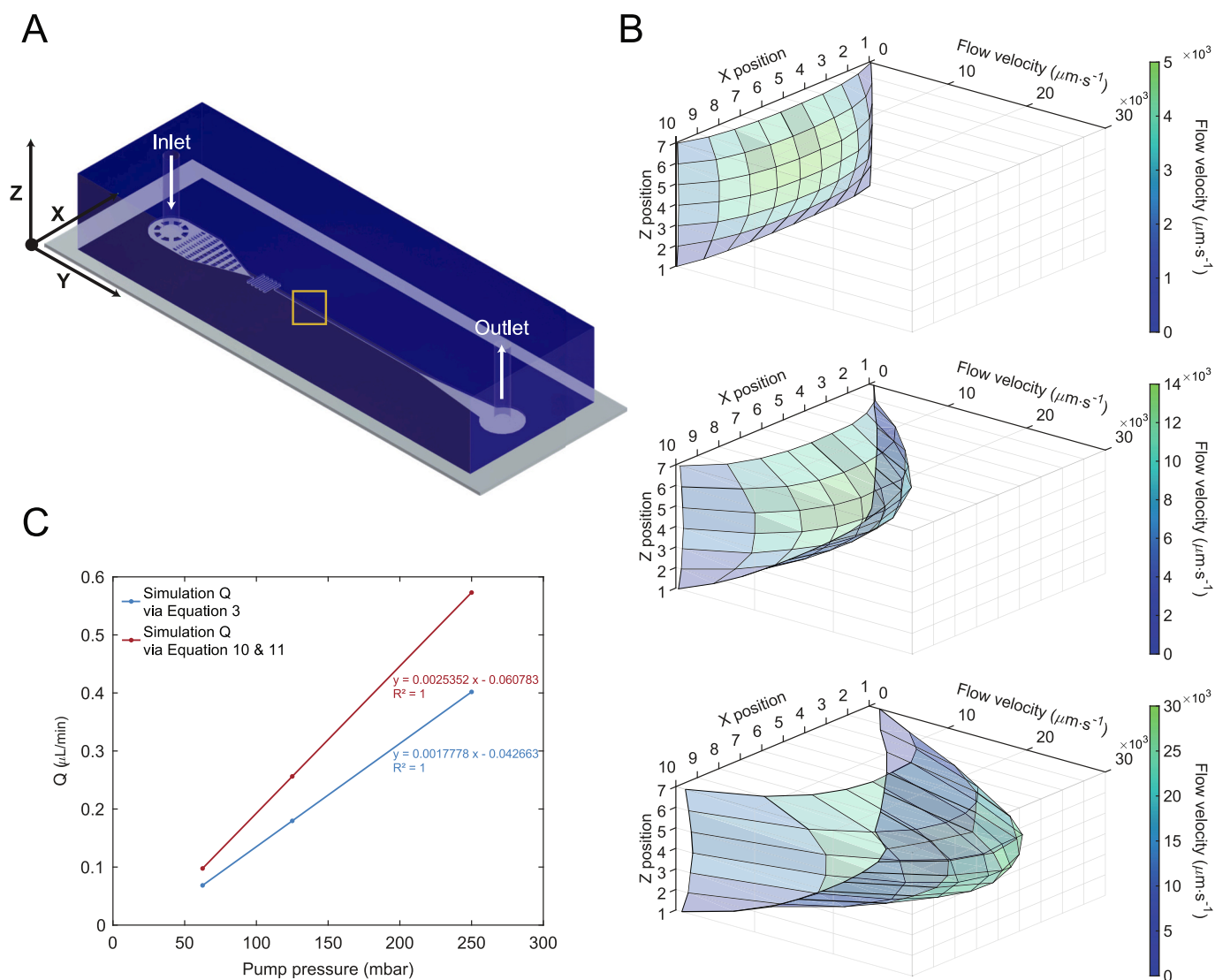
Fig. 1. In silico flow velocities in a microfluidic chip at different virtual pump pressures. A) Design of the microfluidic chip with measurement region highlighted with orange square; B) Simulation of 3D flow rate at 62.5 mbar, 125 mbar and 250 mbar virtual pump pressure; C) Volumetric flow rate (y-axis) dependence on pump pressure (x-axis).

3. Results and discussion

3.1. In silico microfluidic flow profiles

Single-particle-based fluorescence studies allow studying in-population molecular heterogeneity and determining population distributions of molecular properties. Single-molecule confocal spectroscopy techniques most often rely on Brownian motion to sample molecules that randomly diffuse through a static confocal volume. Unfortunately, dense supramolecular complexes do not exhibit significant translational motion, but rather have the propensity to sink, rendering classical diffusion-based single-molecule methodologies cumbersome if not impractical. To circumvent this problem, we turned to microfluidics and designed a PDMS microfluidic chip (Fig. 1A) with channels that are 30 μm wide, 15 μm high, and 27.4 mm long (inlet to outlet). In these microfluidic chips, the sample flows in through a single inlet before reaching a dust filter composed of increasingly smaller gaps that filter out particles bigger than the smallest channel dimensions, which would otherwise clog the microchannel. The sample then flows through a serpentine feature, increasing travel time and mixing before it reaches the measurement region (highlighted with an orange square in Fig. 1A). Finally, it exits the microfluidic chip through the outlet, where the sample is collected again.

First, to predict the flow velocities of an aqueous solution in the channel, we performed simulations at the different virtual pump pressures: 62.5, 125, and 250 mbar. Considering the 24.5 cm difference in height between the pressure pump and the microfluidic chip, the inlet pressures were adjusted to the theoretical pressure at the chip inlet using Bernoulli's equation, resulting in theoretical inlet pressures of 38.5, 101, and 226 mbar. The flow velocities were retrieved for different heights and in ten spots spanning the width of the channel. Flow simulations are shown in Fig. 1B. The flow profile exhibited a similar shape for all pressures, with velocities increasing from the walls to the middle of the channel, where the highest flow rates were observed. Moreover, at higher pressures, the flow profile exhibited a steeper velocity increase towards the middle of the channel, which is expected for laminar flow in straight microchannels [38]. The flow rates corresponding to the simulations performed at virtual pump pressures of 62.5, 125, and 250 mbar could be calculated with Eq. (3), resulting in flow rates of 0.062, 0.180 and 0.402 μL/min (Fig. 1C, blue), respectively. The simulated flow rate graphs (Fig. 1C, blue) show that the simulated data intercepts the x-axis at 24 mbar, reflecting the theoretical pressure difference due to the height between the pump and the microfluidic chip.

For the determination of the volumetric flow rates in experimental data, we propose the use of a simplified approach. Briefly, the average velocity of the parabolic flow profile at the centreline $v\left(y, \frac{h}{2}\right)$ is calculated via Eq. (10), and the volumetric flow rate is then determined using Eq. (11), where the flow rate is defined by the average velocity (v_{avg}) and the cross-sectional area (A) of the microfluidic channel. However, this method tends to overestimate the experimental flow rates due to the fact that v_{avg} is calculated along the centreline, where we can also find the maximum velocity. To address this, we applied this approach to the simulated data ($Q_{sim.\,2}$) to estimate the systematic bias (c) for Eq. (11) when determining flow rates for experimental data using v_{avg} at one height $\left(y, \frac{h}{2}\right)$. We found that the use of Eq. (11) led to an overestimation of the flow rate by an average of 43% (Fig. 1C, red). Henceforth, the systematic bias (c) is employed in Eq. (11) for all further calculations of the experimental volumetric flow rates.

A critical parameter for microfluidics is the Reynolds number (Re). This dimensionless parameter reports the ratio of inertial forces to viscous forces and predicts the fluid flow pattern as either laminar or turbulent. Using the average flow velocities derived from the simulated data and the hydraulic diameter derived from Eq. (6), it was possible to calculate Reynolds numbers using Eq. (4) for the channel in the microfluidic chip at the different pump pressures (S. Table 2). At 62.5, 125, and 250 mbar virtual pump pressure, the Reynold numbers ($Re_{Sim.}$) were 0.0502, 0.1422, and 0.3189, respectively. All Reynold numbers in the different conditions are lower than 1, meaning that at these pump pressures, the flow is laminar; thus, fluid elements move along orderly parallel streamlines, and the viscous forces dominate the inertial forces. By using Eq. (6) and the results of the flow rates of the in silico data for different virtual pump pressures, the hydraulic resistance ($R_{h\,sim.}$) for the fluid flowing through the microfluidic channel could be calculated. The hydraulic resistance should remain constant across different measurements within the same microfluidic chip using the same fluid, which is observed in the simulated data (S. Table 3). At 62.5, 125, and 250 mbar virtual pump pressure, the hydraulic resistances ($R_{h\,sim.}$) were indeed invariable (3.375×10^{15}, 3.367×10^{15}, and 3.373×10^{15} Pa· s/m³, respectively).

In conclusion, the in silico results revealed expected flow velocity profiles under various virtual pump pressures, which provided a better understanding of the microchannel device used later in experimental conditions. Reynold numbers calculated from the in silico data indicate laminar flow for all pressure conditions. Additionally, we determined a simple correction for calculating volumetric flow rates from experimental data using input v_{avg} data measured only along the centreline of a microfluidic chip.

3.2. Fluorescence microscopy microfluidic flow characterisation

In the next step, we experimentally microfabricated and subsequently characterised the microfluidic chip with the use of single-molecule sensitive fluorescence microscopy. We developed microfluidic chips made out of PDMS, a transparent material compatible with fluorescence spectroscopy methodologies and, therefore, desirable for the applications used here. A sample of 80 nM ATTO 488 was run through the channel, which provided a homogeneous distribution of fluorescence signal, creating ideal conditions for the characterisation of the microchip chip. We first acquired a 3D z-stack image to allow determining the overall dimensions of the channel. As seen in S. Fig. 1, fluorescence appears only from a very defined region corresponding to the channel. Furthermore, from size analysis of the z-stack's cross-section and orthogonal views (Fig. 2A) of four separate chips, it was possible to retrieve an average channel width of 32.0 μm and channel height of 15.2 μm, which is very close to the chip's design.

Next, flow velocities were determined via AD-FCS, as exemplified in Fig. 2B. We consecutively performed ten measurements along the width of the channel at 6 different z-positions. Fluorescence intensity time traces were recorded using a single-photon sensitive array detector, from which intensity fluctuations in 9 pairs of non-adjacent detectors within the 3 inner detector element rings (Fig. 2B, right, light grey and coloured elements) were bidirectionally cross-correlated along three distinct axes (0°-180°, 300°-120°, 240°-60°) to construct average pair-cross-correlation curves per axis. Examples of correlation curves obtained for ATTO 488 solution under flow at a pump pressure of 125 mbar are shown in Fig. 2C. It is clear that different correlation functions were obtained when correlating the same detection units in opposite directions, e.g. the correlation function in the 300° to 120° direction (i.e. in the direction of the flow) was different than that in the 120° to 300° direction (opposite to the flow). This difference is expected for a solution under flow. Qualitatively, the most pronounced correlation is seen when cross-correlating units from 300° to 120° and 240° to 60°, suggesting that the dye translates along this specific direction. Also, it is noticeable that the cross-correlation curves between 0°-180° are not exactly the same, indicating that the microfluidic channel is not perfectly perpendicular to the correlation pairs, 0° to 180° and 180° to 0°. Next, when measuring flow FCS data of ATTO 488 at pump pressures of 62.5, 125, and 250 mbar, we observed that correlation curves obtained with higher pump pressures decay at shorter lag times, revealing the faster flow
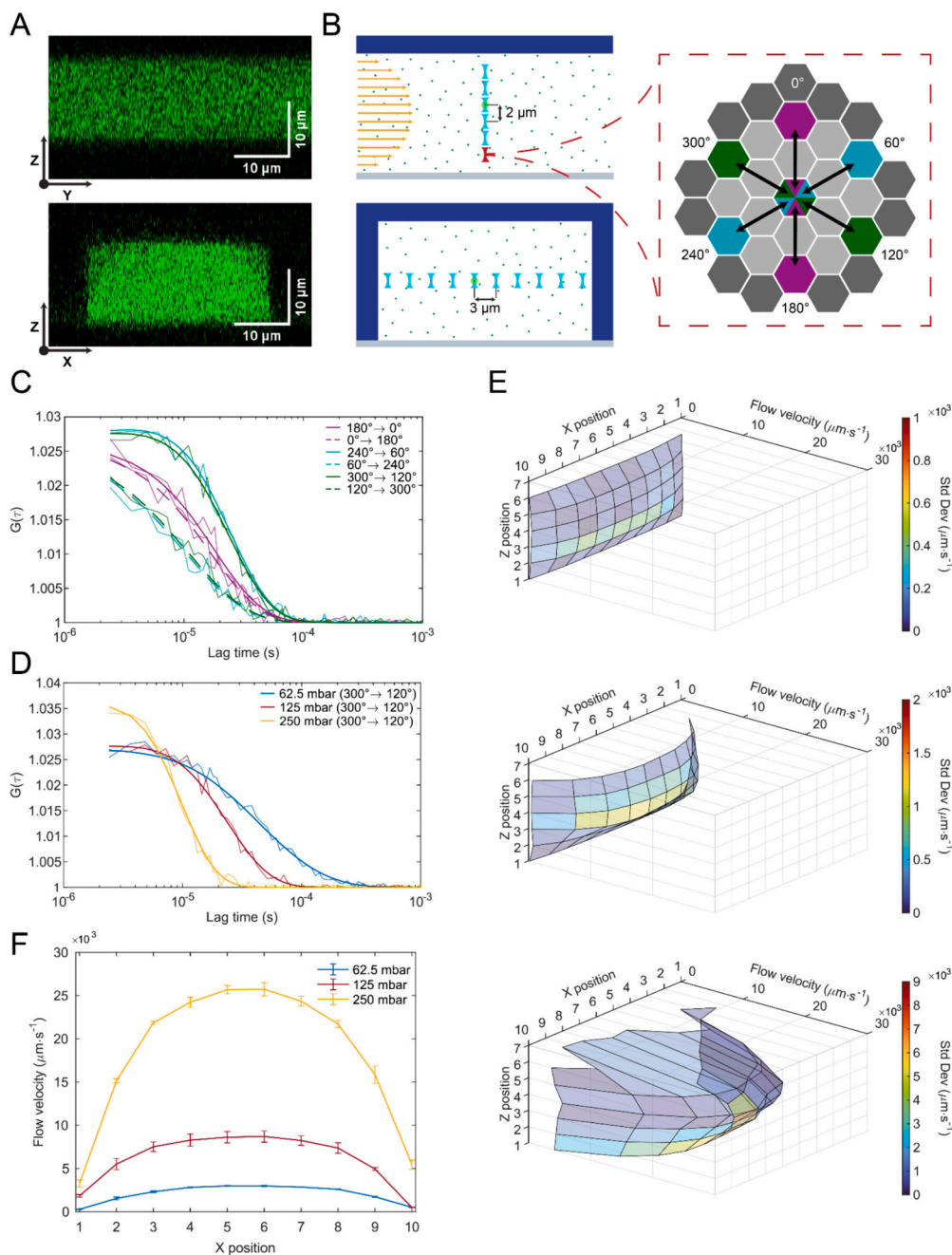
Fig. 2. Microfluidic flow velocity. A) Orthogonal and cross-section view of microfluidic chip loaded with 80 nM ATTO 488 solution, B) Representation of FCS methodology for flow measurement along the height and width of the channel, with array-detector. Matching coloured detection pairs are bidirectionally cross-correlated. For visualisation purposes, only 2 pair-correlations per direction are shown, while in reality, 9 different pairs can be formed per direction. C) Cross-correlation curves between detection units for ATTO488 flow at 125 mbar pump pressure at x,z position (7,4) colour coded for the three different axes, D) Correlation curves of ATTO 488 at different pump pressures at x,z position (7,4), E) 3D flow rate at 62.5 mbar, 125 mbar and 250 mbar pump pressure, F) Flow velocity measured along the channel width and at z position 4. Error bars represent the standard deviation of three measurements using the same microfluidic chip.

velocities of the solution under such conditions (Fig. 2D).

Quantitatively, experimental flow FCS data was fitted to Eq. (9), which revealed both the angle of the flow direction and the local flow velocities in each measurement location. Flow velocities obtained from correlation curves at different z-planes and different spots along the width of the channel are shown in Fig. 2E. The 3-dimensional flow velocities of fluorescent dye in solution at the different pump pressures were rather similar to those observed in the simulations. Here, the calculated volumetric flow rates using Eq. (10) and Eq. (11) averaged over three measurements per pump pressure, 62.5, 125, and 250 mbar, were approximately 0.044, 0.125, and 0.372 μL/min, respectively,

while the volumetric flow rates in the simulations were 0.062, 0.180, and 0.402 μL/min. The variation between simulated and experimental obtained flow velocities is probably attributed to obstructions within the dust filter section of the microfluidic channel, resulting in a slight decrease in the overall flow rate. Alternatively, small movements of the microfluidic chip/microscope stage in x and z during the FCS measurements can also contribute to these variations. The obtained simulated and experimental 3D flow profiles show that even a slight difference in the x, z position can have a great impact on the measured flow velocity. Reynolds numbers (*Re*) for the experimental flow are in agreement with those found for the simulations, indicating that the

experimental flow is laminar and the viscous forces dominate the inertial forces (S. Table 4).

The expected parabolic flow pattern can be better observed in Fig. 2F, where the flow velocities determined at the channel centreline are plotted. We observe that flow velocities of both the simulations and experimentally obtained data do not correspond with the given linear pump pressures (62.5125, 250) as expected due to the difference in height between the pump and the microfluidic channel, which disrupts the linear scaling of the pump pressure at the microfluidic channel. Furthermore, the parabolic flow patterns shown here are similar to those reported before, using similar FCS based techniques [29,39–41]. *P. R. Nicovich & R. M. Dickson (2009)* studied microfluidic flow properties by correlating pairs of pixels in 2D images to reconstitute a 3D flow [39]. *Kuricheti* et al. *(2004)* and *Gösch* et al. *(2000)* applied a classical stationary laser focal volume approach to FCS to obtain a fluorescence correlation curve along the width of the channel, which could be fitted to retrieve flow velocity values [40,41]. *T. J. Arbour & Enderlein J. (2010)* used pair-correlation of a dual laser focal volume positioned at a known distance to determine the flow velocity along the Z axis of the microfluidic chip [29]. The FCS module, in combination with the detector array used here, provides an easy implementation since ten spots can be chosen based on a reference image and are measured in succession. Furthermore, analysis and curve fitting are immediately available in the same software after measurement, providing quick access to flow velocity and direction.

3.3. Droplet flow characterisation

After characterising the channel, measurements with labelled Tau protein were performed. This recombinant protein was previously purified and labelled at the two natural cysteines with Alexa-Fluor 488 maleimide. Since several proteins, Tau included, are prone to adsorb to the glass and PDMS, PLL-g-PEG was pumped through the tubes and channels to passivate all the walls that Tau is in contact with. The flow properties of the protein sample were obtained by pushing 80 nM of monomeric labelled Tau protein through the channel. FCS measurements were taken at the channel height at which the maximum flow velocity was observed previously (Fig. 2F). A shift to longer lag times with lower pump pressures is also seen for all curves, indicating slower flow velocities (Fig. 3A). From such curves we retrieved the parabolic flow velocity curves across the width of the channel and observed that values are consistently slower than those observed with ATTO 488. This difference can be attributed to the use of a PLL-g-PEG passivated microfluidic chip, which can increase the overall resistance of the channel. Expectedly, monomeric Tau flowed at higher flow velocities towards the middle of the channel in all pump pressures used. Similar experiments were performed with a solution containing 50 μM unlabelled Tau, 20 nM labelled Tau, and 15% (w/V) PEG 8000, which forced Tau to undergo liquid-liquid phase separation. In this solution, a dense and a dilute phase coexist in physical equilibrium, though due to the difference in local concentrations, the dense phase appears much brighter (Fig. 3B). In Fig. 3C, the correlation curves of both phases are shown, though obtaining flow velocities from such correlation curves is more complex since two components with inhomogeneous sizes and brightnesses are considered simultaneously. Additionally, the fit model for flow analysis (Eq. (9)) is optimal for particles smaller than the focal detection volume [32], therefore, large and bright biocondensates will likely impact the flow analysis, resulting in an underestimation of flow speed (Fig. 3C). To determine the flow velocity of the dilute phase in this complex LLPS sample a digital 'dust' filter was applied. This allowed the removal of the bright spikes of the biocondensates and, thus, the analysis of the homogeneous dilute phase, as can be seen by the typical-looking correlation curves in Fig. 3D. Compared to monomeric Tau, a further decrease in flow velocity was observed for the dilute phase. Spot-FCS measurements in both the dilute phase and dense phase allowed the unveiling of the viscosity for each phase via Eq. (12). (S. Fig. 2) (SI

Table 5). The introduction of 15% (w/V) of PEG 8000 induces the complex LLPS two-phase system, leading to a viscosity increase in the dilute phase exceeding twice that of water (SI Table 5). This phenomenon may explain the observed slower flow velocities for the dilute phase. Moreover, we noticed that despite the difference in pump pressure, the velocity profiles were closer together and did not change linearly with the pressure. Having access to the flow velocity of the dilute phase without the signal contribution of the dense phase allowed us to study the hydraulic resistance for monomeric tau flow and LLPS-dilute phase flow.

To compare the monomeric Tau flow with the dilute phase of the Tau LLPS sample, we derived the flow rates for both monomeric Tau flow and the dilute phase of Tau using Eq. (10) & Eq. (11) and the systematic bias determined above. Fig. 5A illustrates the flow rate dependence on the pump pressure. It is clear that the monomeric flow rate scales linearly with the pump pressure (Fig. 4A, blue), the plot also intercepts the x-axis at 26 mbar, which is close to the theoretical pressure difference of 24 mbar due to the height between the pump and the microfluidic chip. Flow rates of the dilute phase also increase with increasing pump pressure, though at a slower rate (Fig. 4A, red).

Further analysis of the monomeric and dilute phase flow was done by calculating the hydraulic resistance (R_h). As depicted in Eq. (6), the hydraulic resistance correlates with both the pressure drop across the channel and the volumetric flow rate. As aforementioned, the hydraulic resistance should remain constant during the microfluidic experiments if the fluid characteristics and geometry are unchanged. We observe that the hydraulic resistance for the monomeric Tau solution remains relatively constant (Fig. 4B, blue). In contrast, the calculated values for the hydraulic resistance of the dilute phase show a linear increase in hydraulic resistance towards higher pump pressures (Fig. 4B, red). The overall higher hydraulic resistance of the dilute phase flow compared to the monomeric tau flow may be attributed to the addition of 15% (w/V) PEG 8000 in the LLPS solution, which increases the viscosity of the solution (S. Table 5). Given measurements were consistently taken from high pump pressures to low pump pressures, and that LLPS Tau experiments at all pump pressures were conducted using the same microfluidic chip, we expect that if overall clogging was the major driving force in the increase of hydraulic resistance, it would be observed at the lower pump pressures. Since we observe the opposite, with a linear increase in the hydraulic resistance towards higher pump pressures (Fig. 4B), flow velocities of lower pump pressures approaching the flow velocities of higher pump pressures (Fig. 3D), and no change in fluid characteristics under pressure (S. Fig. 3), we hypothesise that the initial measurements showed a higher resistance due to a greater presence of droplets. This was likely caused by how the pump collects fluid from the bottom of a tube, where larger droplets tend to accumulate due to their faster sinking. As a result, the simultaneous flow of many large droplets through the small channels of the microfluidic chip, especially at the dust filter section at the inlet, may increase the resistance of the fluid flow.

An acquired time-series of a Tau LLPS flow (left panel) and the representative fluorescence intensity time trace (right panel) is shown in Fig. 5A. Here, we see that, due to their higher brightness, droplets passing through the confocal volume lead to spikes in fluorescence intensity, reminiscent of single-molecule bursts observed in confocal burst analysis. Since the employed AD-FCS method allowed us to predefine up to ten spots that span the width of the channel, we could retrieve information about where droplets were most likely to flow through the channel. As expected, at all pump pressures, droplets tended to localise towards the faster flow velocity regions, with a higher occurrence of droplets found near the centre of the channel (Fig. 5A, left panel). This information is crucial for translation to single-molecule experiments in biocondensates under flow as it allows us to place the confocal volume in a position where more biocondensates can be detected. Afterwards, we studied how many droplets/min were detected in the spots of highest occurrence (x-position: 6 & 7) to establish a suitable pressure for future
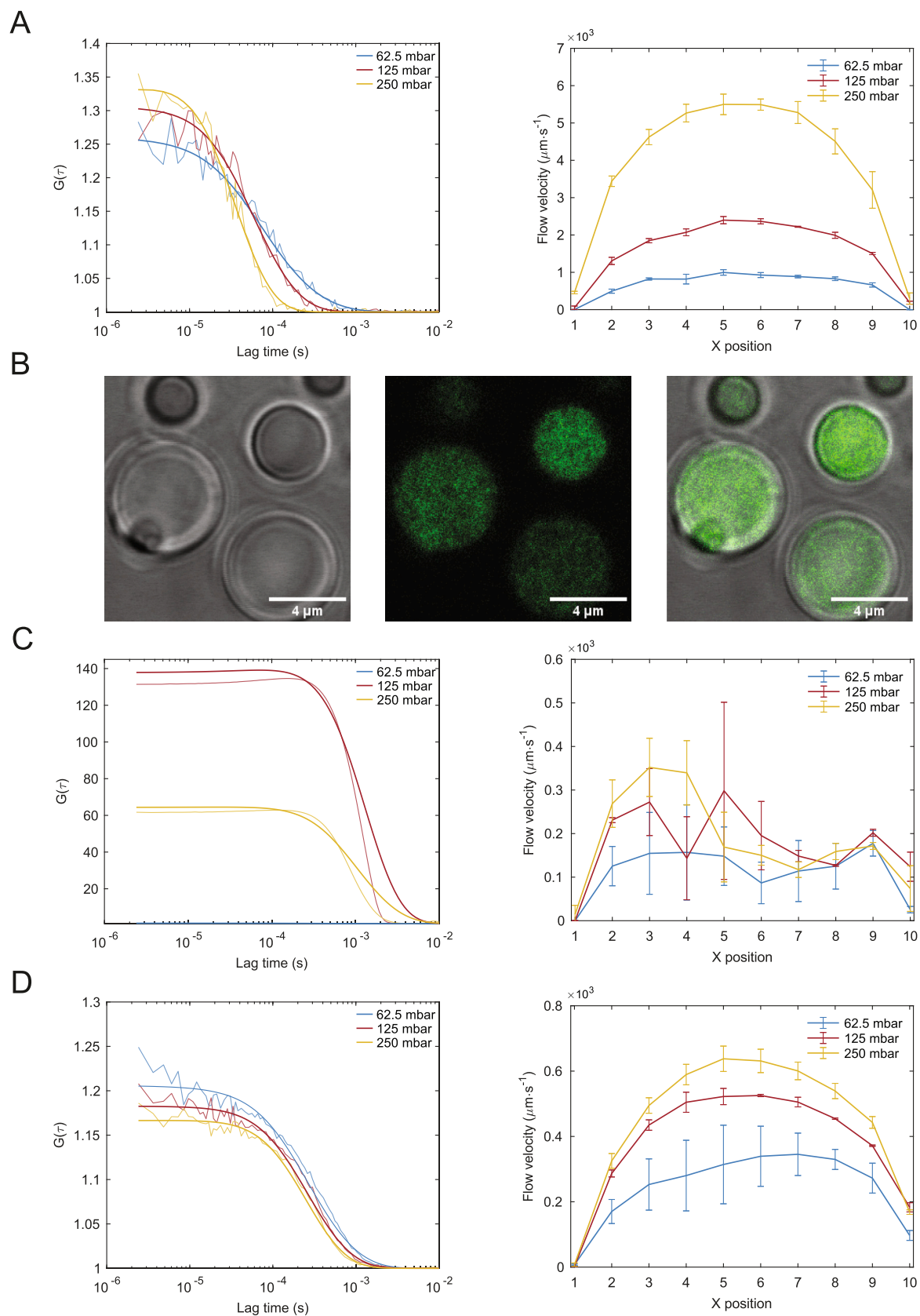
Fig. 3. Flow velocity profiles change under different pump pressures for different Tau solutions. A) Fluorescence correlation curves acquired for a solution of 80 nM monomeric tau at pump pressures of 62.5, 125 and 250 mbar and corresponding flow velocities profiles across the width of the channel at the midpoint height of the channel, B) Transmission and fluorescence images of biocondensates in the LLPS tau sample, C) Velocity profile of Tau LLPS droplets at midpoint height of the channel & D) Dilute phase of the Tau LLPS condensate solution at midpoint height of the channel. Error bars represent the standard deviation of three measurements using the same sample and microfluidic chip.
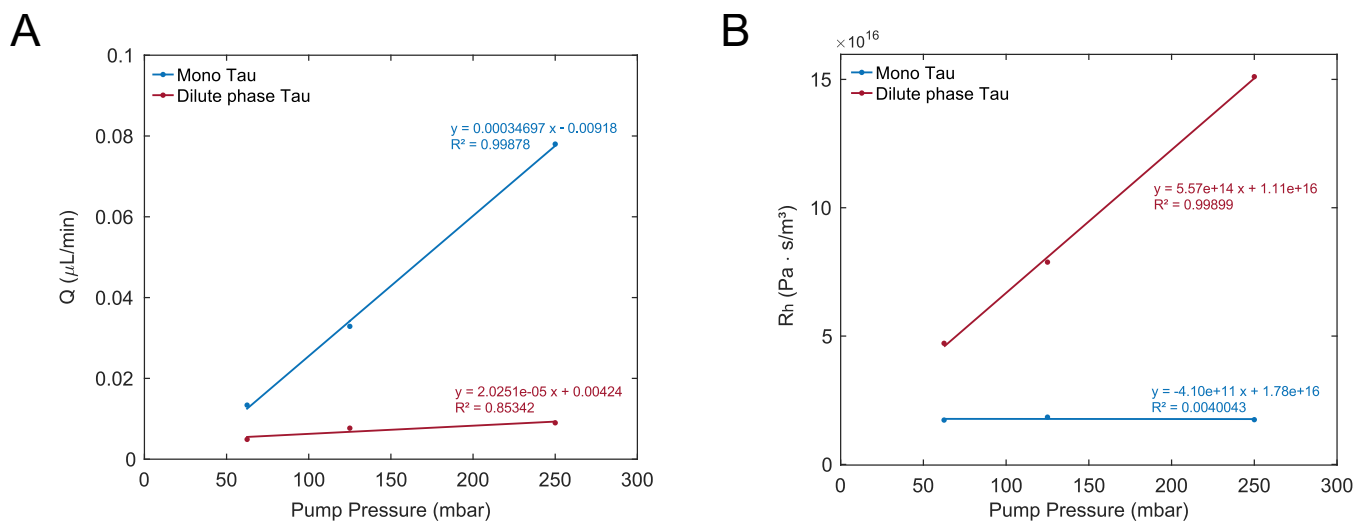
Fig. 4. Experimentally calculated flow parameters of different Tau solutions. A) Volumetric flow rate (y-axis) dependence on pump pressure (x-axis) & B) Hydraulic resistance (y-axis) at different pump pressures (x-axis).

experiments (Fig. 5B). We found that with increasing pump pressure, the number of droplets detected per minute also increased, from 9 to 78 and 1687 droplets/min at 25, 250 and 1000 mbar, respectively. At these higher pump pressures, sampling at faster rates is possible. Furthermore, since biocondensates are typically micrometre-sized, detection of more than one droplet at each time is not expected, and a single molecule regime can be maintained. Importantly, the highest pump pressure used here matches the lowest pressure applied in previous investigations designed to study the effects of pressure in the phase diagram [42,43]. To further examine this under the pressure condition used in this study, we measured the diffusion of ATTO 488 and ATTO 565 dye, freely diffusing in the LLPS solution within a tightly closed channel chamber under pressure. No change in diffusion was observed for either the dilute or dense phases (S. Fig. 3). Therefore, as mentioned before, the fluid characteristics did not change under the pressure conditions used in this study.

Another essential aspect of fluorescence-based single-molecule structural research is the time molecules spend in the confocal volume. The longer a molecule resides in the measurement spot, the more photons can be collected, and thus, the more accurately its behaviour can be studied. With the microfluidic methodology employed here, we aimed to recreate an experimental setup that enables the study of multiparameter fluorescence detection, similar to that of a monomeric protein, therefore, we also determined the effect of different pressure pumps in the burst duration. Burst data was analysed through a home-built script, briefly, an intensity threshold of twice the background noise was set, at which a burst start time was marked. Once the intensity has dropped below the threshold for at least three time bins, a burst end was recorded, and the time difference was used as burst duration. Subsequently, the obtained burst data underwent further analysis and thresholding based on the minimum duration required for a single monomeric Tau molecule to cross the confocal volume diameter (0.412 µm) at each flow velocity for every measurement spot. Therefore, only data with a burst duration exceeding that of a single molecule was considered for analysis.

The impact of pump pressure on the burst duration is illustrated in Fig. 5D. At the lowest pressure, we observe the longest burst durations, correlating directly with the flow velocity of the droplets passing through the confocal volume. The highest average burst duration, 5.092 ms, was measured at 25 mbar, while only an average burst duration of 0.9365 ms was observed at 500 mbar. In a typical single-molecule experiment, proteins remain in the focal plane for approximately 2 ms, providing adequate time to quantify their fluorescence properties [14]. Even though such burst durations shown here align well with the

typical burst durations seen in single-molecule research, we note that these times are obtained for droplets containing more than one labelled protein and thus are not compatible with fluorescence-based intra-droplet single-molecule measurements. Depending on the time scale of the conformational changes, tunable burst durations may be desired. As mentioned above, we show the burst durations of the positions with the highest occurrence of bursts, yet this also means the highest flow velocity. Therefore, longer burst durations can be measured at positions with a lower flow velocity. However, this may result in a reduced number of bursts, consequently prolonging the duration of the experiment (S. Fig. 4). Alternatively, we hypothesise that minor modifications to the microfluidic chip aimed to increase the overall fluid flow resistance will enable flow rates at stable pump pressures that allow long burst durations of biocondensates carrying a single labelled protein.

To describe the flow of particles in a microfluidic channel, the particle Reynold number Re_p must be defined. Therefore, we calculated the Re_p using Eq. (12) for particles with a particle diameter of 1 µm and 10 µm at the different flow conditions (S. Table 6). In all different pressure conditions and particle diameters, we observe that the $Re_p \ll 1$, in this regime, only viscous effects are present. Spherical particles will move along the undisturbed streamlines without any lateral lift forces [36]. The only force experienced by the particles will be the drag force. Because of the low Re_p, particles will flow approximately at the same velocity as the fluid flow [36,44–46]. Therefore, the velocity profile of the dilute phase of Tau (Fig. 3D) could be used to estimate the droplet diameter by converting the Tau droplet burst duration into a distance using Eq. (13).

Converting the burst duration of Tau droplets into droplet diameters reveals minimal variation of droplet diameter across different pressure measurements (Fig. 5E). At pump pressures of 25, 62.5, 125, 250, and 500 mbar, the average droplet diameters were 0.8518, 0.8091, 0.9094, 1.157, and 0.9040 µm, respectively. Via dynamic light scattering (DLS) measurements, we could indeed confirm the presence of 1-µm-sized particles in the Tau LLPS sample (S. Fig. 5). The droplet sizes we report here are smaller than those reported elsewhere generated under similar experimental conditions [10,12]. One explanation for this could be that droplets fuse more efficiently (increasing their size) when they sediment on coverslips prior to imaging, as opposed to our solution based measurements. The similar droplet sizes at different pump pressures indicate that using higher pump pressures may not disturb or disrupt the LLPS droplets.
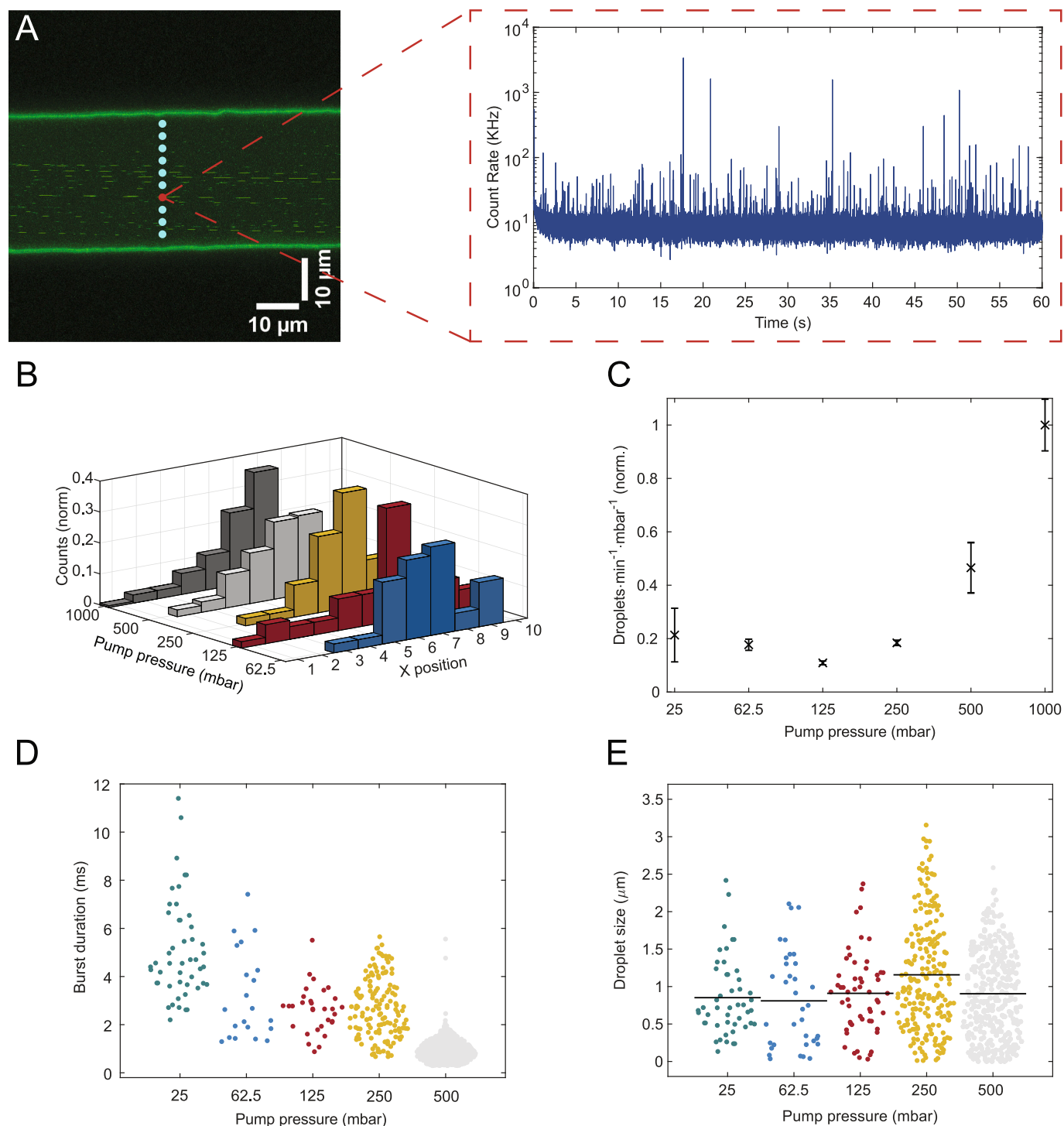
Fig. 5. LLPS-Tau droplets measurement under flow. A) Maximum intensity projection of a time-series of droplets flowing with a fluorescence intensity trace obtained from an AD-FCS measurement at spot 7 B) Histogram of the number of droplets (normalised) over one minute, for all spots and pump pressures, C) Plot of the number of droplets at spot 7 (normalised to the pump pressure) for the different pump pressures, D) Burst duration measured under different flow conditions at positions 6 and 7 in the channel & E) Droplet size determine with use of burst duration (black lines represent average droplet size).

4. Conclusion

In recent years, the inclusion of intrinsically disordered proteins in dynamic supramolecular organisations formed via liquid-liquid phase separation has led to the proposal of this physical process as a potential pathological pathway that ultimately results in several dementias. These diseases are often associated with protein misfolding and aggregation. Understanding the dynamics and intermediate conformations of these

proteins is then crucial in elucidating their fundamental mechanical properties. In this study, we employed a single-channel microfluidic chip and demonstrated the use of a commercially available sub-resolution fluorescence correlation spectroscopy technique. This method allowed a fast and direct characterisation of the channel's physical properties, such as flow velocity and directionality. Our observations confirmed that the experimental flow characteristics align with those predicted by simulations, showing faster flow rates towards the centre of the channel,

typical for laminar flow.

Furthermore, we characterised solutions of Tau protein undergoing LLPS. Our results show the possibility of distinguishing the dense phase from the dilute phase based on the burst duration. This allowed us to identify positions on the channel where droplets are more likely to be found. We further note that the average burst duration window of 0.9365 ms to 5.092 ms obtained for this chip and pump pressures is compatible with molecular dynamics analysis. Even though such burst durations were obtained for biocondensates containing much more than a single labelled molecule, we hypothesise that channel configurations will allow a precise flow that is slow to the point where droplets with a single labelled molecule can be sampled for 2 ms or longer. Lastly, we used the obtained burst data and flow velocity data to estimate the diameter of the LLPS Tau condensates and found that Tau droplets retain a similar size at all pump pressures used. We demonstrated the feasibility of characterising droplet diameters via FCS-derived burst data, thereby introducing another approach to analysing LLPS solutions and their corresponding phase diagrams.

With the work shown here, we thus initiate and pave the way for a novel approach to studying protein conformational dynamics within condensates.

Funding

Credit authorship contribution statement

Stijn Dilissen: Writing – review & editing, Writing – original draft, Visualization, Software, Methodology, Investigation, Formal analysis, Conceptualization. **Pedro L. Silva:** Writing – review & editing, Writing – original draft, Visualization, Software, Methodology, Investigation, Formal analysis, Conceptualization. **Anastasia Smolentseva:** Writing – review & editing, Resources. **Tom Kache:** Writing – review & editing, Software. **Ronald Thoelen:** Writing – review & editing. **Jelle Hendrix:** Writing – review & editing, Writing – original draft, Supervision, Conceptualization.

Declaration of competing interest

Jelle Hendrix reports financial support was provided by Research Foundation Flanders. Stijn Dilissen reports financial support was provided by Research Foundation Flanders. Tom Kache reports financial support was provided by Research Foundation Flanders. If there are other authors, they declare that they have no known competing financial interests or personal relationships that could have appeared to influence the work reported in this paper.

Data availability

All data and materials are available upon request.

Acknowledgements

Appendix A. Supplementary data

Supplementary data to this article can be found online at https://doi.org/10.1016/j.bbagen.2024.130673.

References

[1] A.A. Hyman, C.A. Weber, F. Jülicher, Liquid-liquid phase separation in biology, Annu. Rev. Cell Dev. Biol. 30 (2014) 39–58.

[2] S. Alberti, D. Dormann, Liquid-liquid phase separation in disease, Annu. Rev. Genet. 53 (2019) 171–194.

[3] B. Wang, L. Zhang, T. Dai, Z. Qin, H. Lu, L. Zhang, F. Zhou, Liquid-liquid phase separation in human health and diseases, Signal Transduct. Target. Ther. 6 (2021) 290.

[4] J. Hervy, D.J. Bicout, Dynamical decoration of stabilized-microtubules by tau-proteins, Sci. Rep. 9 (2019) 12473.

[5] X.-H. Li, J.A. Culver, E. Rhoades, Tau binds to multiple tubulin dimers with helical structure, J. Am. Chem. Soc. 137 (2015) 9218–9221.

[6] A.W.P. Fitzpatrick, B. Falcon, S. He, A.G. Murzin, G. Murshudov, H.J. Garringer, R. A. Crowther, B. Ghetti, M. Goedert, S.H.W. Scheres, Cryo-EM structures of tau filaments from Alzheimer's disease, Nature 547 (2017) 185–190.

[7] B. Falcon, W. Zhang, A.G. Murzin, G. Murshudov, H.J. Garringer, R. Vidal, R. A. Crowther, B. Ghetti, S.H.W. Scheres, M. Goedert, Structures of filaments from Pick's disease reveal a novel tau protein fold, Nature 561 (2018) 137–140.

[8] W. Zhang, A. Tarutani, K.L. Newell, A.G. Murzin, T. Matsubara, B. Falcon, R. Vidal, H.J. Garringer, Y. Shi, T. Ikeuchi, S. Murayama, B. Ghetti, M. Hasegawa, M. Goedert, S.H.W. Scheres, Novel tau filament fold in corticobasal degeneration, Nature 580 (2020) 283–287.

[9] S.H.W. Scheres, B. Ryskeldi-Falcon, M. Goedert, Molecular pathology of neurodegenerative diseases by cryo-EM of amyloids, Nature 621 (2023) 701–710.

[10] S. Wegmann, B. Eftekharzadeh, K. Tepper, K.M. Zoltowska, R.E. Bennett, S. Dujardin, P.R. Laskowski, D. MacKenzie, T. Kamath, C. Commins, C. Vanderburg, A.D. Roe, Z. Fan, A.M. Molliex, A. Hernandez-Vega, D. Muller, A. A. Hyman, E. Mandelkow, J.P. Taylor, B.T. Hyman, Tau protein liquid-liquid phase separation can initiate tau aggregation, EMBO J. 37 (2018), https://doi.org/10.15252/embj.201798049.

[11] J. Hochmair, C. Exner, M. Franck, A. Dominguez-Baquero, L. Diez, H. Brognaro, M. L. Kraushar, T. Mielke, H. Radbruch, S. Kaniyappan, S. Falke, E. Mandelkow, C. Betzel, S. Wegmann, Molecular crowding and RNA synergize to promote phase separation, microtubule interaction, and seeding of tau condensates, EMBO J. 41 (2022) e108882.

[12] N.M. Kanaan, C. Hamel, T. Grabinski, B. Combs, Liquid-liquid phase separation induces pathogenic tau conformations in vitro, Nat. Commun. 11 (2020) 2809.

[13] J. Wen, L. Hong, G. Krainer, Q.-Q. Yao, T.P.J. Knowles, S. Wu, S. Perrett, Conformational expansion of tau in condensates promotes irreversible aggregation, J. Am. Chem. Soc. 143 (2021) 13056–13064.

[14] G. Agam, C. Gebhardt, M. Popara, R. Mächtel, J. Folz, B. Ambrose, N. Chamachi, S. Y. Chung, T.D. Craggs, M. de Boer, D. Grohmann, T. Ha, A. Hartmann, J. Hendrix, V. Hirschfeld, C.G. Hübner, T. Hugel, D. Kammerer, H.-S. Kang, A.N. Kapanidis, G. Krainer, K. Kramm, E.A. Lemke, E. Lerner, E. Margeat, K. Martens, J. Michaelis, J. Mitra, G.G. Moya Muñoz, R.B. Quast, N.C. Robb, M. Sattler, M. Schlierf, J. Schneider, T. Schröder, A. Sefer, P.S. Tan, J. Thurn, P. Tinnefeld, J. van Noort, S. Weiss, N. Wendler, N. Zijlstra, A. Barth, C.A.M. Seidel, D.C. Lamb, T. Cordes, Reliability and accuracy of single-molecule FRET studies for characterization of structural dynamics and distances in proteins, Nat. Methods 20 (2023) 523–535.

[15] W. Zheng, G.L. Dignon, N. Jovic, X. Xu, R.M. Regy, N.L. Fawzi, Y.C. Kim, R.B. Best, J. Mittal, Molecular details of protein condensates probed by microsecond long atomistic simulations, J. Phys. Chem. B 124 (2020) 11671–11679.

[16] N. Galvanetto, M.T. Ivanović, A. Chowdhury, A. Sottini, M.F. Nüesch, D. Nettels, R. B. Best, B. Schuler, Extreme dynamics in a biomolecular condensate, Nature 619 (2023) 876–883.

[17] G. Gharib, İ. Bütün, Z. Muganlı, G. Kozalak, İ. Namlı, S.S. Sarraf, V.E. Ahmadi, E. Toyran, A.J. van Wijnen, A. Koşar, Biomedical applications of microfluidic devices: a review, Biosensors 12 (2022), https://doi.org/10.3390/bios12111023.

[18] M. Linsenmeier, M.R.G. Kopp, S. Stavrakis, A. de Mello, P. Arosio, Analysis of biomolecular condensates and protein phase separation with microfluidic technology, Biochim. Biophys. Acta, Mol. Cell Res. 1868 (2021) 118823.

[19] A.-G. Niculescu, C. Chircov, A.C. Bîrcă, A.M. Grumezescu, Fabrication and applications of microfluidic devices: a review, Int. J. Mol. Sci. 22 (2021), https://doi.org/10.3390/ijms22042011.

[20] N.A. Erkamp, R. Qi, T.J. Welsh, T.P.J. Knowles, Microfluidics for multiscale studies of biomolecular condensates, Lab Chip 23 (2022) 9–24.

[21] K. Rhine, S. Skanchy, S. Myong, Single-molecule and ensemble methods to probe RNP nucleation and condensate properties, Methods 197 (2022) 74–81.

[22] P. Pokhrel, S. Jonchhe, W. Pan, H. Mao, Single-molecule dissection of liquid-liquid phase transitions, J. Am. Chem. Soc. 145 (2023) 17143–17150.

[23] D. Magde, E.L. Elson, W.W. Webb, Fluorescence correlation spectroscopy. II. An experimental realization, Biopolymers 13 (1974) 29–61.

[24] L. Yu, Y. Lei, Y. Ma, M. Liu, J. Zheng, D. Dan, P. Gao, A comprehensive review of fluorescence correlation spectroscopy, Front. Phys. 9 (2021), https://doi.org/10.3389/fphy.2021.644450.

[25] D. Magde, W.W. Webb, E.L. Elson, Fluorescence correlation spectroscopy. III. Uniform translation and laminar flow, Biopolymers 17 (1978) 361–376.

[26] M.A. Digman, C.M. Brown, P. Sengupta, P.W. Wiseman, A.R. Horwitz, E. Gratton, Measuring fast dynamics in solutions and cells with a laser scanning microscope, Biophys. J. 89 (2005) 1317–1327.

[27] M.A. Digman, E. Gratton, Imaging barriers to diffusion by pair correlation functions, Biophys. J. 97 (2009) 665–673.

[28] M. Brinkmeier, K. Dörre, J. Stephan, M. Eigen, Two-beam cross-correlation: a method to characterize transport phenomena in micrometer-sized structures, Anal. Chem. 71 (1999) 609–616.

[29] T.J. Arbour, J. Enderlein, Application of dual-focus fluorescence correlation spectroscopy to microfluidic flow-velocity measurement, Lab Chip 10 (2010) 1286–1292.

[30] L. Scipioni, L. Lanzanó, A. Diaspro, E. Gratton, Comprehensive correlation analysis for super-resolution dynamic fingerprinting of cellular compartments using the Zeiss Airyscan detector, Nat. Commun. 9 (2018) 5120.

[31] E. Slenders, M. Castello, M. Buttafava, F. Villa, A. Tosi, L. Lanzanò, S.V. Koho, G. Vicidomini, Confocal-based fluorescence fluctuation spectroscopy with a SPAD array detector, Light Sci. Appl. 10 (2021) 31.

[32] Annette Bergter, Hanna Reuter, Georg Wieser, Stanislav Kalinin, Volodymyr Kudryavtsev, Dieter Huhse, Follow Dynamic Biological Processes and Reveal Spatial Molecular Characteristics, ZEISS Dynamics Profiler, Carl Zeiss Microscopy GmbH, 2023.

[33] H.A. Stone, Introduction to fluid dynamics for microfluidic flows, in: H. Lee, R. M. Westervelt, D. Ham (Eds.), CMOS Biotechnology, Springer, US, Boston, MA, 2007, pp. 5–30.

[34] H. Bruus, Governing Equations in Microfluidics, 2014.

[35] C.M. Hedgepeth, L.J. Conrad, J. Zhang, H.C. Huang, V.M. Lee, P.S. Klein, Activation of the Wnt signaling pathway: a molecular mechanism for lithium action, Dev. Biol. 185 (1997) 82–91.

[36] D. Huber, A. Oskooei, X. Casadevall, I. Solvas, A. de Mello, G.V. Kaigala, Hydrodynamics in cell studies, Chem. Rev. 118 (2018) 2042–2079.

[37] Peter Kapusta, PicoQuant GmbH, Absolute Diffusion Coefficients: Compilation of Reference Data for FCS Calibration, 2010.

[38] F. Pisapia, W. Balachandran, M. Rasekh, Organ-on-a-chip: design and simulation of various microfluidic channel geometries for the influence of fluid dynamic parameters, NATO Adv, Sci. Inst. Ser. E Appl. Sci. 12 (2022) 3829.

[39] P.R. Nicovich, R.M. Dickson, Three-dimensional flow mapping in microfluidic channels with Widefield cross-correlation microscopy, Isr. J. Chem. 49 (2010) 293–301.

[40] K.K. Kuricheti, V. Buschmann, K.D. Weston, Application of fluorescence correlation spectroscopy for velocity imaging in microfluidic devices, Appl. Spectrosc. 58 (2004) 1180–1186.

[41] M. Gosch, H. Blom, J. Holm, T. Heino, R. Rigler, Hydrodynamic flow profiling in microchannel structures by single molecule fluorescence correlation spectroscopy, Anal. Chem. 72 (2000) 3260–3265.

[42] R. Kitahara, R. Yamazaki, F. Ide, S. Li, Y. Shiramasa, N. Sasahara, T. Yoshizawa, Pressure-jump kinetics of liquid-liquid phase separation: comparison of two different condensed phases of the RNA-binding protein, fused in sarcoma, J. Am. Chem. Soc. 143 (2021) 19697–19702.

[43] S. Li, T. Yoshizawa, R. Yamazaki, A. Fujiwara, T. Kameda, R. Kitahara, Pressure and temperature phase diagram for liquid-liquid phase separation of the RNA-binding protein fused in sarcoma, J. Phys. Chem. B 125 (2021) 6821–6829.

[44] D.D. Carlo, D. Irimia, R.G. Tompkins, M. Toner, Continuous inertial focusing, ordering, and separation of particles in microchannels, Proc. Natl. Acad. Sci. 104 (2007) 18892–18897.

[45] A. Sohrabi Kashani, M. Packirisamy, Efficient low shear flow-based trapping of biological entities, Sci. Rep. 9 (2019) 5511.

[46] P. Tabeling, Introduction to Microfluidics, Oxford University Press, 2023.

[47] M.L. Huber, R.A. Perkins, A. Laesecke, D.G. Friend, J.V. Sengers, M.J. Assael, I. N. Metaxa, E. Vogel, R. Mareš, K. Miyagawa, New international formulation for the viscosity of H2O, J. Phys. Chem. Ref. Data Monogr. 38 (2009) 101–125.